Measurement of ϕ-meson production at forward rapidity in $p+p$ collisions at $\sqrt{s}=510$ GeV and its energy dependence from $\sqrt{s}=200$ GeV to 7 TeV

A. Adare,[12] C. Aidala,[42] N. N. Ajitanand,[59,*] Y. Akiba,[54,55,†] R. Akimoto,[11] M. Alfred,[23] N. Apadula,[28,60] Y. Aramaki,[54] H. Asano,[34,54] E. T. Atomssa,[60] T. C. Awes,[50] B. Azmoun,[7] V. Babintsev,[24] A. Bagoly,[16] M. Bai,[6] N. S. Bandara,[41] B. Bannier,[60] K. N. Barish,[8] S. Bathe,[5,55] A. Bazilevsky,[7] M. Beaumier,[8] S. Beckman,[12] R. Belmont,[12,42] A. Berdnikov,[57] Y. Berdnikov,[57] D. Black,[8] M. Boer,[37] J. S. Bok,[48] K. Boyle,[55] M. L. Brooks,[37] J. Bryslawskyj,[5,8] H. Buesching,[7] V. Bumazhnov,[24] S. Campbell,[13,28] V. Canoa Roman,[60] C.-H. Chen,[55] C. Y. Chi,[13] M. Chiu,[7] I. J. Choi,[25] J. B. Choi,[10,*] T. Chujo,[63] Z. Citron,[65] M. Connors,[20,55] M. Csanád,[16] T. Csörgő,[17,66] T. W. Danley,[49] A. Datta,[47] M. S. Daugherity,[1] G. David,[7,60] K. DeBlasio,[47] K. Dehmelt,[60] A. Denisov,[24] A. Deshpande,[55,60] E. J. Desmond,[7] L. Ding,[28] A. Dion,[60] J. H. Do,[67] A. Drees,[60] K. A. Drees,[6] J. M. Durham,[37] A. Durum,[24] A. Enokizono,[54,56] H. En'yo,[54] S. Esumi,[63] B. Fadem,[43] W. Fan,[60] N. Feege,[60] D. E. Fields,[47] M. Finger,[9] M. Finger, Jr.,[9] S. L. Fokin,[33] J. E. Frantz,[49] A. Franz,[7] A. D. Frawley,[19] Y. Fukuda,[63] C. Gal,[60] P. Gallus,[14] P. Garg,[3,60] H. Ge,[60] F. Giordano,[25] A. Glenn,[36] Y. Goto,[54,55] N. Grau,[2] S. V. Greene,[64] M. Grosse Perdekamp,[25] Y. Gu,[59] T. Gunji,[11] H. Guragain,[20] T. Hachiya,[54,55] J. S. Haggerty,[7] K. I. Hahn,[18] H. Hamagaki,[11] S. Y. Han,[18] J. Hanks,[60] S. Hasegawa,[29] T. O. S. Haseler,[20] X. He,[20] T. K. Hemmick,[60] J. C. Hill,[28] K. Hill,[12] A. Hodges,[20] R. S. Hollis,[8] K. Homma,[22] B. Hong,[32] T. Hoshino,[22] N. Hotvedt,[28] J. Huang,[7,37] S. Huang,[64] Y. Ikeda,[54] K. Imai,[29] Y. Imazu,[54] J. Imrek,[15] M. Inaba,[63] A. Iordanova,[8] D. Isenhower,[1] D. Ivanishchev,[53] B. V. Jacak,[60] S. J. Jeon,[44] M. Jezghani,[20] Z. Ji,[60] J. Jia,[7,59] X. Jiang,[37] B. M. Johnson,[7,20] E. Joo,[32] K. S. Joo,[44] V. Jorjadze,[60] D. Jouan,[51] D. S. Jumper,[25] J. H. Kang,[67] J. S. Kang,[21] S. Karthas,[60] D. Kawall,[41] A. V. Kazantsev,[33] J. A. Key,[47] V. Khachatryan,[60] A. Khanzadeev,[53] K. Kihara,[63] C. Kim,[8,32] D. H. Kim,[18] D. J. Kim,[30] E.-J. Kim,[10] H.-J. Kim,[67] M. Kim,[58] M. H. Kim,[32] Y. K. Kim,[21] D. Kincses,[16] E. Kistenev,[7] J. Klatsky,[19] D. Kleinjan,[8] P. Kline,[60] T. Koblesky,[12] M. Kofarago,[16,66] J. Koster,[55] D. Kotov,[53,57] S. Kudo,[63] B. Kurgyis,[16] K. Kurita,[56] M. Kurosawa,[54,55] Y. Kwon,[67] R. Lacey,[59] J. G. Lajoie,[28] A. Lebedev,[28] K. B. Lee,[37] S. H. Lee,[28,60] M. J. Leitch,[37] M. Leitgab,[25] Y. H. Leung,[60] N. A. Lewis,[42] X. Li,[37] S. H. Lim,[37,67] M. X. Liu,[37] S. Lökös,[16] D. Lynch,[7] Y. I. Makdisi,[6] M. Makek,[65,68] A. Manion,[60] V. I. Manko,[33] E. Mannel,[7] H. Masuda,[56] M. McCumber,[37] P. L. McGaughey,[37] D. McGlinchey,[12,37] C. McKinney,[25] A. Meles,[48] M. Mendoza,[8] B. Meredith,[13] W. J. Metzger,[17] Y. Miake,[63] A. C. Mignerey,[40] D. E. Mihalik,[60] A. J. Miller,[1] A. Milov,[65] D. K. Mishra,[4] J. T. Mitchell,[7] I. Mitrankov,[57] G. Mitsuka,[31,55] S. Miyasaka,[54,62] S. Mizuno,[54,63] P. Montuenga,[25] T. Moon,[67] D. P. Morrison,[7] S. I. Morrow,[64] T. V. Moukhanova,[33] T. Murakami,[34,54] J. Murata,[54,56] A. Mwai,[59] K. Nagai,[62] S. Nagamiya,[31,54] K. Nagashima,[22] J. L. Nagle,[12] M. I. Nagy,[16] I. Nakagawa,[54,55] H. Nakagomi,[54,63] K. Nakano,[54,62] C. Nattrass,[61] P. K. Netrakanti,[4] M. Nihashi,[22,54] T. Niida,[63] R. Nouicer,[7,55] T. Novák,[17,66] N. Novitzky,[30,60] A. S. Nyanin,[33] E. O'Brien,[7] C. A. Ogilvie,[28] J. D. Orjuela Koop,[12] J. D. Osborn,[42] A. Oskarsson,[38] K. Ozawa,[31,63] R. Pak,[7] V. Pantuev,[26] V. Papavassiliou,[48] J. S. Park,[58] S. Park,[54,58,60] S. F. Pate,[48] L. Patel,[20] M. Patel,[28] J.-C. Peng,[25] W. Peng,[64] D. V. Perepelitsa,[7,12,13] G. D. N. Perera,[48] D. Yu. Peressounko,[33] C. E. PerezLara,[60] J. Perry,[28] R. Petti,[7,60] C. Pinkenburg,[7] R. Pinson,[1] R. P. Pisani,[7] A. Pun,[49] M. L. Purschke,[7] P. V. Radzevich,[57] J. Rak,[30] I. Ravinovich,[65] K. F. Read,[50,61] D. Reynolds,[59] V. Riabov,[46,53] Y. Riabov,[53,57] D. Richford,[5] T. Rinn,[28] N. Riveli,[49] D. Roach,[64] S. D. Rolnick,[8] M. Rosati,[28] Z. Rowan,[5] J. G. Rubin,[42] J. Runchey,[28] N. Saito,[31] T. Sakaguchi,[7] H. Sako,[29] V. Samsonov,[46,53] M. Sarsour,[20] K. Sato,[63] S. Sato,[29] S. Sawada,[31] B. Schaefer,[64] B. K. Schmoll,[61] K. Sedgwick,[8] J. Seele,[55] R. Seidl,[54,55] A. Sen,[28,61] R. Seto,[8] P. Sett,[4] A. Sexton,[40] D. Sharma,[60] I. Shein,[24] T.-A. Shibata,[54,62] K. Shigaki,[22] M. Shimomura,[28,45] P. Shukla,[4] A. Sickles,[7,25] C. L. Silva,[37] D. Silvermyr,[38,50] B. K. Singh,[3] C. P. Singh,[3] V. Singh,[3] M. J. Skoby,[42] M. Slunečka,[9] R. A. Soltz,[36] W. E. Sondheim,[37] S. P. Sorensen,[61] I. V. Sourikova,[7] P. W. Stankus,[50] M. Stepanov,[41,*] S. P. Stoll,[7] T. Sugitate,[22] A. Sukhanov,[7] T. Sumita,[54] J. Sun,[60] J. Sziklai,[66] A. Takahara,[11] A. Takeda,[45] A. Taketani,[54,55] K. Tanida,[29,55,58] M. J. Tannenbaum,[7] S. Tarafdar,[64,65] A. Taranenko,[46,59] G. Tarnai,[15] R. Tieulent,[39] A. Timilsina,[28] T. Todoroki,[54,55,63] M. Tomášek,[14] H. Torii,[11] C. L. Towell,[1] M. Towell,[1] R. Towell,[1] R. S. Towell,[1] I. Tserruya,[65] Y. Ueda,[22] B. Ujvari,[15] H. W. van Hecke,[37] M. Vargyas,[16,66] S. Vazquez-Carson,[12] J. Velkovska,[64] M. Virius,[14] V. Vrba,[14,27] E. Vznuzdaev,[53] X. R. Wang,[48,55] Z. Wang,[5] D. Watanabe,[22] Y. Watanabe,[54,55] Y. S. Watanabe,[11,31] F. Wei,[48] S. Whitaker,[28] S. Wolin,[25] C. P. Wong,[20] C. L. Woody,[7] M. Wysocki,[50] B. Xia,[49] C. Xu,[48] Q. Xu,[64] L. Xue,[20] S. Yalcin,[60] Y. L. Yamaguchi,[11,55,60] A. Yanovich,[24] P. Yin,[12] J. H. Yoo,[32] I. Yoon,[58] I. Younus,[35] H. Yu,[48,52] I. E. Yushmanov,[33] W. A. Zajc,[13] A. Zelenski,[6] S. Zharko,[57] and L. Zou[8]

(PHENIX Collaboration)

[1]*Abilene Christian University, Abilene, Texas 79699, USA*
[2]*Department of Physics, Augustana University, Sioux Falls, South Dakota 57197, USA*

[3]*Department of Physics, Banaras Hindu University, Varanasi 221005, India*
[4]*Bhabha Atomic Research Centre, Bombay 400 085, India*
[5]*Baruch College, City University of New York, New York, New York, 10010 USA*
[6]*Collider-Accelerator Department, Brookhaven National Laboratory, Upton, New York 11973-5000, USA*
[7]*Physics Department, Brookhaven National Laboratory, Upton, New York 11973-5000, USA*
[8]*University of California-Riverside, Riverside, California 92521, USA*
[9]*Charles University, Ovocný trh 5, Praha 1, 116 36, Prague, Czech Republic*
[10]*Chonbuk National University, Jeonju, 561-756, Korea*
[11]*Center for Nuclear Study, Graduate School of Science, University of Tokyo, 7-3-1 Hongo, Bunkyo, Tokyo 113-0033, Japan*
[12]*University of Colorado, Boulder, Colorado 80309, USA*
[13]*Columbia University, New York, New York 10027 and Nevis Laboratories, Irvington, New York 10533, USA*
[14]*Czech Technical University, Zikova 4, 166 36 Prague 6, Czech Republic*
[15]*Debrecen University, H-4010 Debrecen, Egyetem tér 1, Hungary*
[16]*ELTE, Eötvös Loránd University, H-1117 Budapest, Pázmány P. s. 1/A, Hungary*
[17]*Eszterházy Károly University, Károly Róbert Campus, H-3200 Gyöngyös, Mátrai út 36, Hungary*
[18]*Ewha Womans University, Seoul 120-750, Korea*
[19]*Florida State University, Tallahassee, Florida 32306, USA*
[20]*Georgia State University, Atlanta, Georgia 30303, USA*
[21]*Hanyang University, Seoul 133-792, Korea*
[22]*Hiroshima University, Kagamiyama, Higashi-Hiroshima 739-8526, Japan*
[23]*Department of Physics and Astronomy, Howard University, Washington, D.C. 20059, USA*
[24]*IHEP Protvino, State Research Center of Russian Federation, Institute for High Energy Physics, Protvino, 142281, Russia*
[25]*University of Illinois at Urbana-Champaign, Urbana, Illinois 61801, USA*
[26]*Institute for Nuclear Research of the Russian Academy of Sciences, prospekt 60-letiya Oktyabrya 7a, Moscow 117312, Russia*
[27]*Institute of Physics, Academy of Sciences of the Czech Republic, Na Slovance 2, 182 21 Prague 8, Czech Republic*
[28]*Iowa State University, Ames, Iowa 50011, USA*
[29]*Advanced Science Research Center, Japan Atomic Energy Agency, 2-4 Shirakata Shirane, Tokai-mura, Naka-gun, Ibaraki-ken 319-1195, Japan*
[30]*Helsinki Institute of Physics and University of Jyväskylä, P.O.Box 35, FI-40014 Jyväskylä, Finland*
[31]*KEK, High Energy Accelerator Research Organization, Tsukuba, Ibaraki 305-0801, Japan*
[32]*Korea University, Seoul, 02841, Korea*
[33]*National Research Center "Kurchatov Institute," Moscow, 123098 Russia*
[34]*Kyoto University, Kyoto 606-8502, Japan*
[35]*Physics Department, Lahore University of Management Sciences, Lahore 54792, Pakistan*
[36]*Lawrence Livermore National Laboratory, Livermore, California 94550, USA*
[37]*Los Alamos National Laboratory, Los Alamos, New Mexico 87545, USA*
[38]*Department of Physics, Lund University, Box 118, SE-221 00 Lund, Sweden*
[39]*IPNL, CNRS/IN2P3, Univ Lyon, Université Lyon 1, F-69622, Villeurbanne, France*
[40]*University of Maryland, College Park, Maryland 20742, USA*
[41]*Department of Physics, University of Massachusetts, Amherst, Massachusetts 01003-9337, USA*
[42]*Department of Physics, University of Michigan, Ann Arbor, Michigan 48109-1040, USA*
[43]*Muhlenberg College, Allentown, Pennsylvania 18104-5586, USA*
[44]*Myongji University, Yongin, Kyonggido 449-728, Korea*
[45]*Nara Women's University, Kita-uoya Nishi-machi Nara 630-8506, Japan*
[46]*National Research Nuclear University, MEPhI, Moscow Engineering Physics Institute, Moscow, 115409, Russia*
[47]*University of New Mexico, Albuquerque, New Mexico 87131, USA*
[48]*New Mexico State University, Las Cruces, New Mexico 88003, USA*
[49]*Department of Physics and Astronomy, Ohio University, Athens, Ohio 45701, USA*
[50]*Oak Ridge National Laboratory, Oak Ridge, Tennessee 37831, USA*
[51]*IPN-Orsay, Univ. Paris-Sud, CNRS/IN2P3, Université Paris-Saclay, BP1, F-91406, Orsay, France*
[52]*Peking University, Beijing 100871, People's Republic of China*
[53]*PNPI, Petersburg Nuclear Physics Institute, Gatchina, Leningrad region, 188300, Russia*
[54]*RIKEN Nishina Center for Accelerator-Based Science, Wako, Saitama 351-0198, Japan*
[55]*RIKEN BNL Research Center, Brookhaven National Laboratory, Upton, New York 11973-5000, USA*

[56]Physics Department, Rikkyo University, 3-34-1 Nishi-Ikebukuro, Toshima, Tokyo 171-8501, Japan
[57]Saint Petersburg State Polytechnic University, St. Petersburg, 195251 Russia
[58]Department of Physics and Astronomy, Seoul National University, Seoul 151-742, Korea
[59]Chemistry Department, Stony Brook University, SUNY, Stony Brook, New York 11794-3400, USA
[60]Department of Physics and Astronomy, Stony Brook University, SUNY, Stony Brook, New York 11794-3800, USA
[61]University of Tennessee, Knoxville, Tennessee 37996, USA
[62]Department of Physics, Tokyo Institute of Technology, Oh-okayama, Meguro, Tokyo 152-8551, Japan
[63]Tomonaga Center for the History of the Universe, University of Tsukuba, Tsukuba, Ibaraki 305, Japan
[64]Vanderbilt University, Nashville, Tennessee 37235, USA
[65]Weizmann Institute, Rehovot 76100, Israel
[66]Institute for Particle and Nuclear Physics, Wigner Research Centre for Physics, Hungarian Academy of Sciences (Wigner RCP, RMKI) H-1525 Budapest 114, POBox 49, Budapest, Hungary
[67]Yonsei University, IPAP, Seoul 120-749, Korea
[68]Department of Physics, Faculty of Science, University of Zagreb, Bijenička c. 32 HR-10002 Zagreb, Croatia

(Received 6 October 2017; published 9 November 2018; corrected 16 November 2018)

The PHENIX experiment at the Relativistic Heavy Ion Collider has measured the differential cross section of $\phi(1020)$-meson production at forward rapidity in $p+p$ collisions at $\sqrt{s}=510$ GeV via the dimuon decay channel. The partial cross section in the rapidity and p_T ranges $1.2<|y|<2.2$ and $2<p_T<7$ GeV/c is $\sigma_\phi=[2.28\pm0.09(\text{stat})\pm0.14(\text{syst})\pm0.27(\text{norm})]\times10^{-2}$ mb. The energy dependence of σ_ϕ ($1.2<|y|<2.2, 2<p_T<5$ GeV/c) is studied using the PHENIX measurements at $\sqrt{s}=200$ and 510 GeV and the Large Hadron Collider measurements at $\sqrt{s}=2.76$ and 7 TeV. The experimental results are compared to various event generator predictions (PYTHIA6, PYTHIA8, PHOJET, AMPT, EPOS3, and EPOS-LHC).

DOI: 10.1103/PhysRevD.98.092006

I. INTRODUCTION

The $\phi(1020)$-vector-meson production in $p+p$ collisions was intensively studied by various experiments at different colliding energies and in different rapidity ranges [1–18]. It is the lightest bound state of s and $\bar{s}$ quarks and is considered a good probe to study strangeness production in $p+p$ collisions. Production of ϕ mesons from an initial nonstrange colliding system, such as $p+p$ collisions, is substantially suppressed in comparison to ω and ρ vector mesons due to the Okubo-Zweig-Iizuka rule [19–21]. The ϕ-meson production at low transverse momentum is dominated by soft processes and is sensitive to the hadronization mechanism, while hard processes become dominant at higher transverse momentum. In $p+p$ collisions, the production of strangeness is in general not well described by generators such as PYTHIA, which tend to underestimate the production of strange particles [10, 22–24]. The study of ϕ-meson production in $p+p$ collisions is an important tool to study QCD, providing data to tune phenomenological QCD models in which an interplay is mandatory between perturbative QCD calculations, used in particular for hard parton production dominant at higher p_T, and phenomenological QCD models, needed to describe the nonperturbative hadronization into strange hadrons like the ϕ meson.

In addition, recently, a long-range near-side angular correlation was observed in $p+p$ collisions at LHC energies [25–27], which led to the observation of collectivity in $p+p$ collisions [28]. This observation generated various explanations [29], including those based on the color-glass-condensate model [30], and collective hydrodynamic flow [31] or color reconnection [32,33]. Being the heaviest easily accessible meson made of light quarks, ϕ-meson production provides the largest lever arm accessible to study effects that scale with mass, as should be the case for collective effects [34].

The study of ϕ-meson production in $p+p$ collisions can be an important tool to gain insight into new phenomena, such as long-range angular correlations, that would have a direct impact in the field of relativistic heavy-ion collisions. The ϕ-meson production is an excellent observable to

*Deceased.
†PHENIX Spokesperson: akiba@rcf.rhic.bnl.gov

probe the strangeness enhancement in the quark-gluon plasma created in heavy-ion collisions [35–37].

We report the ϕ-meson-production cross section measured in $p+p$ collisions at $\sqrt{s}=510$ GeV. The analysis uses a data sample of 144.6 pb^{-1} of integrated luminosity obtained by the PHENIX experiment in 2013. The cross section is averaged over the rapidity (y) interval $1.2<|y|<2.2$ and reported in several bins of transverse momentum (p_T) in the range $2<p_T<7$ GeV/c. The results are compared to several model predictions [24,34,38–41] and to the measurements previously reported by the PHENIX experiment at $\sqrt{s}=200$ GeV [15] and by the LHC experiments measuring the ϕ-meson-production cross section at forward rapidity at $\sqrt{s}=2.76$ and 7 TeV [10–13,17]. Measurements from experiments at the Relativistic Heavy Ion Collider (RHIC) and the LHC allow extracting the energy dependence of the ϕ-meson-production cross section in the rapidity range $1.2<y<2.2$, which provides information to further constrain model predictions.

II. EXPERIMENTAL SETUP

A complete description of the PHENIX detector can be found in Ref. [42]. The results presented here are obtained by measuring the ϕ meson via its $\mu^+\mu^-$ decay channel using both PHENIX muon spectrometers covering forward and backward pseudorapidities, $1.2<|\eta|<2.2$, and the full azimuth.

Each muon arm spectrometer comprises hadron absorbers, a muon tracker (MuTr), which resides in a radial field magnet, and a muon identifier (MuID). The absorbers are situated in front of the MuTr to provide hadron (mostly pion and kaon) rejection and are built of 19 cm of copper, 60 cm of iron, and 36.2 cm of stainless steel. The MuTr comprises three sets of cathode strip chambers in a radial magnetic field with an integrated bending power of 0.8 Tesla meters. The final component is the MuID, which has five alternating steel absorbers and Iarocci tubes to further reduce the number of punch-through hadrons misidentified as muons. Muon candidates are identified by reconstructed tracks in the MuTr matched to MuID tracks that penetrate through to the last MuID plane.

Another detector system relevant to this analysis is the beam-beam counter (BBC), comprising two arrays of 64 Čerenkov counters, located on both sides of the interaction point and covering the pseudorapidity $3.1<|\eta|<3.9$. The BBC system is used to measure the $p+p$ collision vertex position along the beam axis ($z_{\rm vtx}$) with 2 cm resolution and to provide the minimum bias (MB) trigger.

III. DATA ANALYSIS

The results presented here are based on the data sample collected by PHENIX during the 2013 $p+p$ run at $\sqrt{s}=510$ GeV. The BBC counters provide the MB trigger, which requires at least one hit in each of the BBCs. Events, in coincidence with the MB trigger, containing a muon pair within the acceptance of the spectrometer are selected by the level-1 dimuon trigger requiring that at least two tracks penetrate through the MuID to its last layer. A total of 5.3×10^8 dimuon triggered events are recorded, which corresponds to a sampled integrated luminosity of 144.6 pb^{-1}.

A. Raw yield extraction

A set of quality assurance cuts is applied to the data to select $p+p$ events and muon candidates as well as to improve the signal-to-background ratio. Good $p+p$ events are selected by requiring that the collision occurs in the fiducial interaction region $|z_{\rm vtx}|<30$ cm as measured by the BBC. No selection is made on the event's charged particle multiplicity. The MuTr tracks are matched to the MuID tracks at the first MuID layer in both the position and angle. In addition, the track is required to have more than a minimum number of possible hits in the MuTr (12 out of the maximum 16) and MuID (6 out of the maximum 10), and cuts on the individual track χ^2 values are applied. Furthermore, there is a minimum allowed single muon momentum along the beam axis, p_z, which is reconstructed and energy-loss corrected at the collision vertex, of 2.4 GeV/c corresponding to the momentum cut effectively imposed by the absorbers. Finally, a cut on the χ^2 of the fit to the common vertex of the two candidate tracks near the interaction point is made.

The invariant mass distribution is formed by combining muon candidate tracks of opposite charges. This unlike-sign dimuon spectrum is composed of correlated and uncorrelated pairs. In the low-mass region (below $\approx$1.5 GeV/c^2), the correlated pairs arise from the two-body and Dalitz decays of the light neutral mesons η, ρ, ω, η', and ϕ as well as semimuonic decays of correlated charmed hadrons (and beauty in a negligible contribution). The uncorrelated pairs are mainly coming from semimuonic decays of pions and kaons and punch-through hadrons and form the so-called combinatorial background. The ratio of the ϕ-meson signal over the combinatorial background is of the order of 0.7. This combinatorial background is estimated using two methods: the first one derives the combinatorial background from the distribution formed within the same event by the muon candidates of the same sign (like-sign pairs), and the second one derives the combinatorial background from the pairs formed by muon candidates of opposite charges (unlike-sign pairs) coming from different events (mixed event). The normalization of the mass distribution of the combinatorial background using the same-event like-sign dimuon distributions (N_{++} and N_{--}) is calculated as $N_{\rm CB}=2\sqrt{N_{++}N_{--}}$.

The mixed-event like-sign dimuon mass distribution is normalized to the same-event like-sign combinatorial background distribution in the invariant mass range 0.2–2.5 GeV/c^2. This factor is then used to normalize the mixed-event unlike-sign dimuon mass distribution.

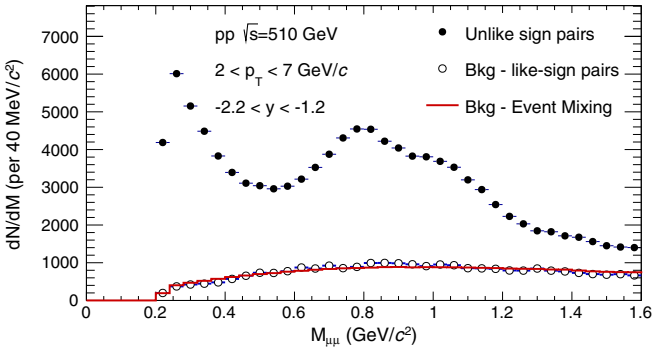

FIG. 1. Unlike-sign dimuon invariant mass spectrum before background subtraction (solid [black] circles) and uncorrelated background distribution estimated using like-sign pairs (open [black] circles) and the event-mixing technique (solid [red] curve).

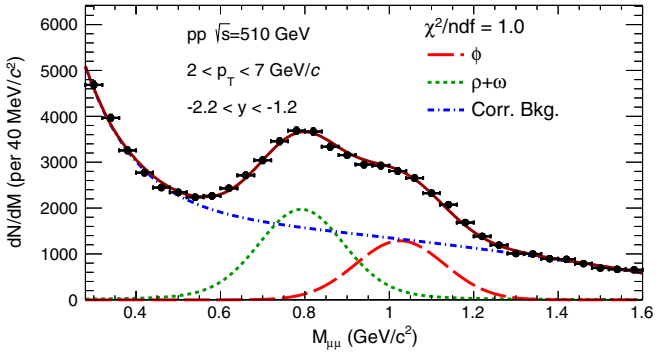

FIG. 2. Unlike-sign signal (solid [black] points) fitted by the sum of three components: ϕ meson (long dash [red] curve), $\rho + \omega$ mesons (short dash [green] curve), and correlated background (dot dash [blue] curve); see the text for details.

Figure 1 shows the unlike-sign dimuon spectrum together with the combinatorial background estimated by both methods that agree within 15% in the invariant mass range of interest ($0.8 < M_{\mu\mu} < 1.3$ GeV/c^2).

The signal invariant mass spectrum is extracted by first subtracting the uncorrelated combinatorial background spectra from the unlike-sign spectra. The signal spectra are then fitted to extract the ϕ contribution. The mass resolution of both muon spectrometers is estimated using Monte Carlo simulation to be 93 (94) MeV/c^2 for the lowest p_T bin ($2 < p_T < 2.5$ GeV/c) and up to 114 (111) MeV/c^2 for the highest p_T bin ($5 < p_T < 7$ GeV/c) for the negative (positive) pseudorapidity muon spectrometer. Those resolutions being greater than the natural widths of the ϕ and ω, the two-body decay of ϕ and ω contributions are described by Gaussians, while the two-body decay of the ρ-meson contribution is described by a Breit-Wigner distribution convoluted with a Gaussian. The contribution from ρ dimuon decay is fixed by the assumption that the production cross sections of ρ and ω are related such as $\sigma_\rho = 1.15 \times \sigma_\omega$, as measured in Ref. [12] and used in previous PHENIX analysis related to ϕ-meson production in the dimuon decay channel [15,43,44]. To evaluate the shape of the correlated background, a PYTHIA [45] MB simulation followed by GEANT3 [46] transport and detector response simulation of the PHENIX detector is performed. The correlated background distribution is found to be well described by an exponential plus a polynomial of first order (χ^2/ndf ≤ 1). To summarize, eight free parameters are needed to describe the signal spectrum: two parameters for the ϕ and $(\omega + \rho)$ signal normalizations, two parameters to describe relative changes of Gaussian widths and central masses with respect to simulation estimates, and four parameters to describe the correlated background distribution and its normalization. The starting values of the free parameters describing the shapes of the different distributions are taken to be the ones from the Monte Carlo simulation.

Figure 2 shows the fit results for the entire p_T range at backward rapidity. Extracted peak positions and widths are found to be in good agreement with Monte Carlo simulations.

B. Detector acceptance and reconstruction efficiency

The product of detector acceptance and reconstruction efficiency, $A\epsilon_{rec}$, of dimuon decays of ϕ mesons is determined by the full event reconstruction of the ϕ-meson signal run through a full GEANT3 simulation of the 2013 PHENIX detector setup and embedded in MB real data. The p_T distribution of the simulated ϕ-meson signal is iteratively reweighted to match the data p_T distribution, the initial p_T distribution being obtained from PYTHIA6 [45] using tune ATLAS_CSC [38]. The embedded simulated events are then reconstructed in the same manner as data with the same cuts applied as in the real data analysis. The $A\epsilon_{rec}$ factor is extracted from the simulation as the ratio of reconstructed ϕ distribution over the generated one in the same kinematic range. Figure 3 shows the $A\epsilon_{rec}$ as a function of ϕ-meson p_T and rapidity. The main sources of the relative difference between both spectrometers $A\epsilon_{rec}$ are different detection efficiencies of the MuTr and MuID systems and different amounts of absorber material.

C. Differential cross section extraction

The p_T-dependent differential cross section is calculated according to

$$\frac{d^2\sigma_\phi}{dp_T dy} = \frac{N_{raw}}{A\epsilon_{rec}\Delta p_T \Delta y BR_{\phi\to\mu^+\mu^-}} \frac{\sigma_{pp}^{BBC}}{\epsilon_{BBC} N_{MB}^{BBC}}, \quad (1)$$

where $BR_{\phi\to\mu^+\mu^-} = (2.87 \pm 0.19) \times 10^{-4}$ is the branching ratio of ϕ decay to dimuon [47]. N_{raw} is the extracted ϕ raw yield for each p_T bin, $N_{MB}^{BBC} = 4.16 \times 10^{12}$ is the number of sampled MB events. The BBC trigger samples a cross section of $\sigma_{pp}^{BBC} = 32.5 \pm 3.2$ mb in $p + p$ collisions,

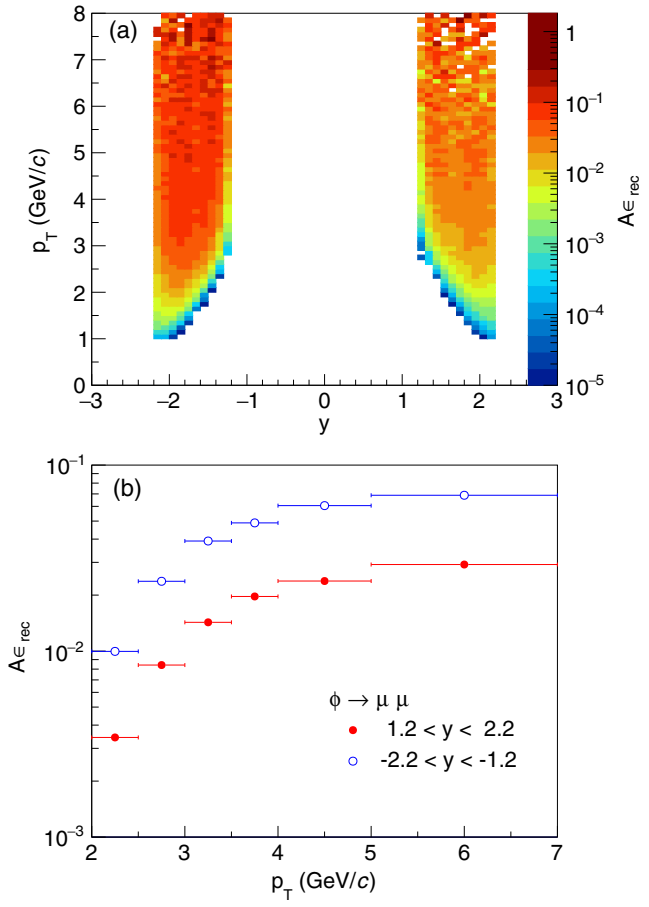

FIG. 3. $A\epsilon_{rec}$ for ϕ detection in forward ($1.2 < y < 2.2$) and backward ($-2.2 < y < -1.2$) muon spectrometers (a) in the p_T-rapidity plane and (b) integrated in rapidity per spectrometer for each p_T bin considered in the analysis.

according to Vernier scans; however, it samples a larger fraction of the cross section when the collision includes a hard scattering process [48]. Studies with high p_T π^0 yields show an increase of the luminosity scanned by the BBC by a factor of $1/\epsilon_{BBC}$, $\epsilon_{BBC} = 0.91 \pm 0.04$ [49]. The inelastic cross sections given by PYTHIA8 [50] for $\sqrt{s} = 500$ and 510 GeV $p + p$ collisions differ by 0.3%; therefore, no correction or additional systematic uncertainty is added.

D. Systematic uncertainties

The main source of systematic uncertainties in the signal extraction comes from the uncorrelated and correlated background distributions used. To estimate this uncertainty, the extracted ϕ raw yields are compared using the following two methods: i) the mixing and like-sign pair methods are separately used for subtraction of uncorrelated background, and ii) the correlated background is fit by an exponential plus first-order polynomial and by an exponential plus second-order polynomial. The extracted ϕ raw yields are consistent among all different fit trials. The quadratic mean of the raw yields extracted from the trials is used as the central value, and the uncertainty on the central value is the quadratic mean of the uncertainties of all the trials. Table I summarizes the systematic uncertainties.

TABLE I. Systematic uncertainties associated with the differential cross section calculation.

Type	Origin	Value
A	Signal extraction	3%–23%
B	$A\epsilon_{rec}$: p_T input distribution	2%–8%
B	$A\epsilon_{rec}$: Rapidity input distribution	3%–5%
B	$A\epsilon_{rec}$: Vertex width fluctuation	3.5%
B	$A\epsilon_{rec}$: MuID hit efficiency	4%
B	$A\epsilon_{rec}$: MuTr hit efficiency	2%
B	$A\epsilon_{rec}$: MuTr tracking efficiency	10%
C	MB trigger efficiency	10%
C	$Br_{\phi\to\mu^+\mu^-}$	6.6%

Type A is a point-to-point uncorrelated uncertainty that allows the data points to move independently with respect to one another and are added in quadrature with statistical uncertainties. A systematic uncertainty equal to the difference between the central and the extreme values of the extracted yields accounts for the systematic uncertainty related to the background description as a whole. The systematic uncertainty associated with the signal extraction method ranges from 3% to 23%, depending on the p_T bin and the muon spectrometer considered (negative/positive rapidity).

Type B is a point-to-point correlated uncertainty that allows the data points to move coherently. To evaluate the $A\epsilon_{rec}$ systematic uncertainty, different p_T and rapidity input distributions of the simulated ϕ mesons are used. The p_T distribution is allowed to vary over the range of the data statistical uncertainty (statistical plus type-A systematics uncertainties added in quadrature; see above), yielding an up to 8% uncertainty. The rapidity distribution shapes given by five generator models (PYTHIA6, PYTHIA8, PHOJET, EPOS3, and EPOS-LHC) are used as input rapidity distributions of the simulated ϕ mesons, resulting in up to 5% uncertainty. The relative systematic uncertainty of acceptance caused by the fluctuation of the vertex width is estimated to be 3.5% [51]. A 4% uncertainty from the measured MuID tube efficiency and a 2% uncertainty from MuTr chamber efficiency are assigned [15]. Simulation parameters are adjusted in order to reproduce the tracking efficiency observed in the data. While the relative tracking efficiency is validated using $J/\psi \to \mu\mu$ data, data-driven evaluation of the absolute tracking efficiency is not available. Therefore, we assign 10% uncertainty for the absolute tracking efficiency as a conservative value [51].

Finally, type C is an overall normalization uncertainty, which allows the data points to move together by a common multiplicative factor. Type C is composed of 10% uncertainty assigned for the BBC cross section and efficiency uncertainties and a 6.6% uncertainty from the measurement of $BR_{\phi\to\mu^+\mu^-}$.

TABLE II. The ϕ-meson-production cross section $d\sigma_\phi/dy$ in $p+p$ collisions at $\sqrt{s}=510$ GeV integrated in the transverse momentum range $2<p_T<7$ GeV/c. The first uncertainty represents the statistical and type-A systematic uncertainties, while the second is the systematic uncertainty of type B, and the third one is the additional ±12% type-C normalization systematic uncertainty.

y range	$d\sigma_\phi/dy$ (mb)
$1.2<y<2.2$	$(2.13\pm0.14\pm0.16\pm0.26)\times10^{-2}$
$-2.2<y<-1.2$	$(2.46\pm0.12\pm0.18\pm0.30)\times10^{-2}$
$1.2<\lvert y\rvert<2.2$	$(2.28\pm0.09\pm0.14\pm0.27)\times10^{-2}$

IV. RESULTS

The p_T-differential cross section is calculated independently for each muon arm, and then the results are combined using the best-linear-unbiased-estimate method [52]. The p_T integrated ($2<p_T<7$ GeV/c) cross section $d\sigma_\phi/dy$ is given in Table II. Results obtained using the two muon spectrometers are consistent within uncertainties. Combining both arm results, the integrated cross section in the kinematic range $2<p_T<7$ GeV/c and $1.2<|y|<2.2$ is $\sigma_\phi=2.28\pm0.09(\text{stat})\pm0.14(\text{syst})\times10^{-2}$ mb, to which a 12% normalization uncertainty applies.

The ϕ-meson-differential cross section as a function of p_T measured in $p+p$ collisions at $\sqrt{s}=510$ GeV is shown in Fig. 4 and listed in Table III. The data points are bin shifted in p_T using the Lafferty and Wyatt method [53] to correct for the finite width of the p_T bins.

The data are fitted by a Tsallis function [54] with a resulting $\chi^2/\text{ndf}=0.66$. The results are compared to calculations performed using six different generator models: PYTHIA6 [45] using tune ATLAS_CSC [38], PYTHIA 8.210 [50] using tune Monash2013 [24], PHOJET 1.12 [39], EPOS 3.117 [34], EPOS-LHC [40], and AMPT v1.26 [41]. Data and models are compared as the ratio of the model prediction over the Tsallis fit of the data.

The AMPT simulation is done with the default AMPT model version 1.26 (without string melting), in which the initial conditions are determined by HIJING [55]. Parton scattering is done using Zhang's parton-cascade model [56]. The hadronization is accomplished using the Lund string fragmentation model [57,58]. The final-state hadronic interactions are based on "a relativistic transport" model [59]. We used the set of parameters tabulated in Ref. [60] describing both the charged particle distribution and elliptic flow measured in Au + Au collisions at the RHIC. The Lund string fragmentation parameters are $a=0.5$ and $b=0.9$ GeV^{-2}, the QCD coupling constant is $\alpha_s=0.33$, and the screening mass is $\mu=3.2$ fm^{-1}, leading to a parton-scattering cross section of 1.5 mb. Besides their production from the fragmentation of excited strings in the initial collisions, ϕ mesons can also be produced and absorbed from hadronic matter via various

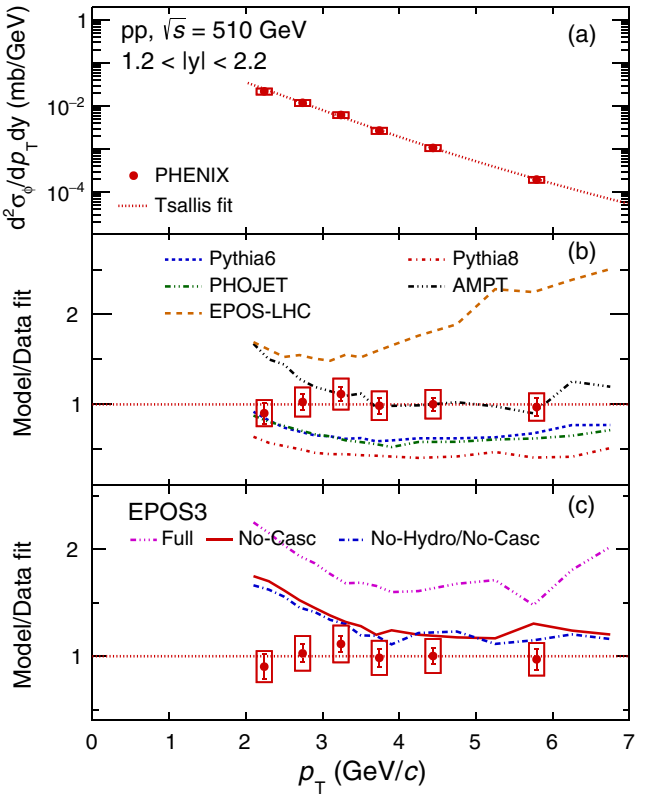

FIG. 4. (a) $d^2\sigma_\phi/dp_Tdy$ measurements in $p+p$ collisions at $\sqrt{s}=510$ GeV fitted by a Tsallis function. Error bars represent the statistical uncertainty, and the boxes represent the type-B and type-C systematic uncertainties added in quadrature. (b) and (c) Comparison between the data and predictions of six models (PYTHIA6 using the tune ATLAS_CSC, PYTHIA8 using tune MONASH2013, PHOJET 1.12, EPOS-LHC, AMPT v1.26, and EPOS 3.117) shown as the ratio of the model to the data fitted by a Tsallis function. (c) The data are compared to EPOS3 predictions using three different options of the model (see the text for details).

TABLE III. The ϕ-meson-differential-production cross section $d^2\sigma_\phi/dp_Tdy$ for $1.2<|y|<2.2$ in $p+p$ collisions at $\sqrt{s}=510$ GeV. $\tilde{p}_T$ is the p_T at which the data point is plotted (see the text for details). The first uncertainty represents the statistical and type-A systematic uncertainties, while the second is the systematic uncertainty of type B, and the third one is the additional ±12% type-C normalization systematic uncertainty.

p_T range (GeV/c)	$\tilde{p}_T$ (GeV/c)	$d^2\sigma_\phi/dp_Tdy$ [mb/(GeV/c)]
2.0–2.5	2.24	$(2.16\pm0.17\pm0.23\pm0.26)\times10^{-2}$
2.5–3.0	2.74	$(1.20\pm0.05\pm0.12\pm0.14)\times10^{-2}$
3.0–3.5	3.24	$(6.26\pm0.36\pm0.61\pm0.75)\times10^{-3}$
3.5–4.0	3.74	$(2.70\pm0.20\pm0.30\pm0.32)\times10^{-3}$
4.0–5.0	4.44	$(1.06\pm0.07\pm0.11\pm0.13)\times10^{-3}$
5.0–7.0	5.79	$(1.97\pm0.19\pm0.20\pm0.24)\times10^{-4}$

hadronic reactions (baryon-baryon, meson-baryon, and meson-meson scatterings) [41].

The EPOS3 model includes, in addition to the description of the initial scattering based on a Gribov-Regge approach [61], a viscous hydrodynamic expansion of the created system followed by a hadronization phase and a final-state hadronic cascade using the URQMD model [62,63]. In EPOS3, the hydrodynamic evolution and the hadronic cascade can be turned on or off, separately. The so-called Full version of EPOS3 includes hydrodynamic expansion of the created system followed by a final-state hadronic cascade. The EPOS3 No-Casc version does not include the final-state hadronic cascade, and No-Hydro/No-Casc has both the hydrodynamic and the final-state hadronic cascade turned off. The EPOS-LHC calculation presented in Fig. 4 is performed, including a parametrized viscous hydrodynamic expansion of the created partonic system.

As shown in panels (b) and (c) of Fig. 4, the experimental data are better reproduced by the AMPT model and by EPOS3 without the hadronic cascade. The EPOS3 Full and EPOS-LHC overestimate the ϕ-meson production, and PHOJET and PYTHIA models tend to underestimate it by a factor of 2. A previous study of the MONASH2013 tune of PYTHIA8 showed that the calculated transverse-momentum spectra of ϕ mesons overestimates the experimental data at very soft momenta (below ~500 MeV/c) and underestimates it at higher momenta, the overall yield of ϕ mesons being correctly reproduced [24].

Additional calculations using the AMPT model with string melting (version 2.26) were performed. The ϕ-meson-production yield was found to be a factor of 2 higher than the one extracted using the default AMPT model with approximately the same p_T dependence. For clarity, those calculations are not shown in Fig. 4.

V. ENERGY DEPENDENCE OF ϕ-MESON PRODUCTION

The PHENIX experiment previously measured the ϕ-meson cross section at forward rapidity and for $1 < p_T < 7$ GeV/c in $p+p$ collisions at $\sqrt{s} = 200$ GeV [15]. At the LHC, the ALICE experiment measured the ϕ-meson-production cross section via its dimuon decay channel in $p+p$ collisions at forward rapidity $2.5 < y < 4.0$ and for $1 < p_T < 5$ GeV/c at $\sqrt{s} = 2.76$ TeV [17] and 7 TeV [12]. Measurement of the ϕ-meson production was also performed via the K^+K^- decay channel at midrapidity $|y| < 0.5$ and for $0.4 < p_T < 6$ GeV/c at $\sqrt{s} = 7$ TeV [13]. The LHCb experiment measured the inclusive ϕ-meson-production cross section in the K^+K^- decay channel in the kinematic range $2.44 < y < 4.06$ and $0.6 < p_T < 5$ GeV/c in $p+p$ collisions at $\sqrt{s} = 7$ TeV [10].

Figures 5–8 show comparisons between $\mathrm{d}^2\sigma_\phi/\mathrm{d}p_T\mathrm{d}y$ measurements at forward rapidities done by PHENIX at $\sqrt{s} = 200$ GeV [15], by ALICE at $\sqrt{s} = 2.76$ TeV [17] and 7 TeV [12], and by LHCb at $\sqrt{s} = 7$ TeV [10], respectively, along with model predictions. The AMPT model is in good agreement with the measured cross sections at both RHIC energies but overestimates the production cross section at LHC energies, especially at 7 TeV. The PYTHIA6 and PHOJET calculations at LHC energies are in better agreement with the data than at RHIC energies, in which the models underestimate the measured production cross section. The PYTHIA8 prediction underestimates the cross section for all four energies.

Panels (c) of Figs. 4–8 show the comparison between the measurements fitted by a Tsallis function and EPOS3 using three different model settings (see above for details). The comparison of those results reveals the effect of the hydrodynamic expansion of the partonic system created in $p+p$ collisions and of the final-state hadronic cascade on the ϕ-meson production. The hydrodynamic evolution does not impact the ϕ-meson production at RHIC energies [No-Casc and No-Hydro/No-Casc curves are almost identical on panel (c) of Figs 4–8]. A significant effect appears at $\sqrt{s} = 2.76$ TeV and becomes stronger at 7 TeV, where the ϕ-meson-production cross section increases by a factor of 2 for the p_T range 1–3 GeV/c when turning on the hydrodynamic evolution. The same behavior was already observed for the production of Λ^0, K_s, and $\Xi^\pm$ in $p+p$ collisions at 7 TeV [34], showing that the flow effects increase with the mass of the particle. The final-state

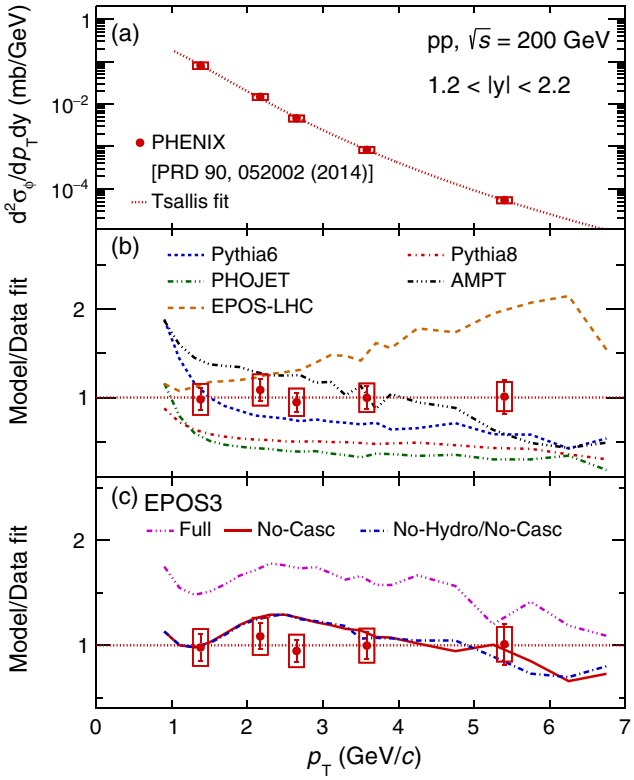

FIG. 5. Same as Fig. 4 for PHENIX measurement at $\sqrt{s} = 200$ GeV [15].

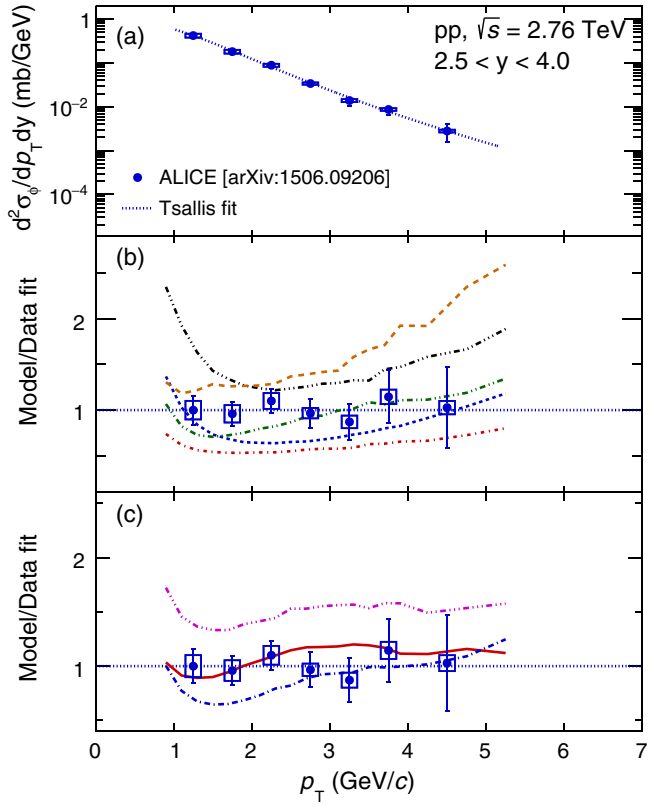

FIG. 6. Same as Fig. 4 for ALICE measurement at $\sqrt{s} = 2.76$ TeV [17].

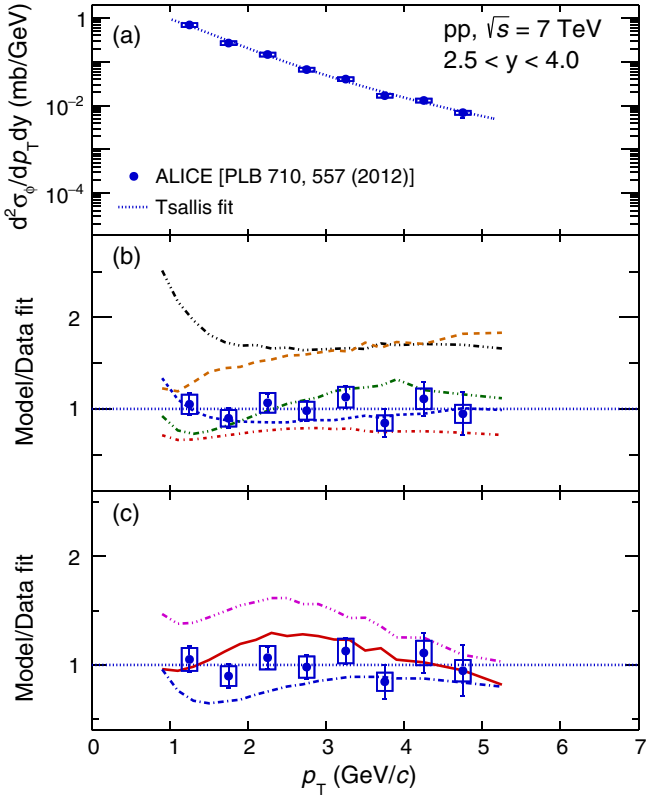

FIG. 7. Same as Fig. 4 for ALICE measurement at $\sqrt{s} = 7$ TeV [12].

hadronic cascade using the URQMD model enhances the ϕ-meson-production cross section in the entire p_T range and for all collision energies. The EPOS3 No-Casc is the best configuration to reproduce the experimental data over the full collision energy range, while the addition of the URQMD hadronic cascade overestimates the ϕ-meson production compared to the experimental data.

In the following, the ϕ-meson cross sections in the forward rapidity range $1.2 < y < 2.2$ at the different measured energies (0.2, 0.51, 2.76, and 7 TeV) are presented. The p_T range is fixed to $2 < p_T < 5$ GeV/c, which is the common range of all experimental measurements.

The cross sections measured by PHENIX in the kinematic range $1.2 < y < 2.2$ and $2 < p_T < 5$ GeV/c are:

(i) $\sigma_\phi(200\ \text{GeV}) = (1.10 \pm 0.17) \times 10^{-2}$ mb,

(ii) $\sigma_\phi(510\ \text{GeV}) = (2.24 \pm 0.32) \times 10^{-2}$ mb,

where the uncertainties correspond to the quadratic sums of the statistical and systematic uncertainties.

The rapidity domains of the LHC measurements are different from those of PHENIX. Accordingly, to compare with PHENIX measurements, the LHC measurements are extrapolated to the same rapidity coverage (i.e., $1.2 < y < 2.2$). The procedure followed here is to fit the LHC data points using the $d\sigma_\phi/dy$ shapes obtained using the different models mentioned above, the only free parameter being the normalization of the simulated $d\sigma_\phi/dy$ distributions. Figure 9 shows the LHC p_T

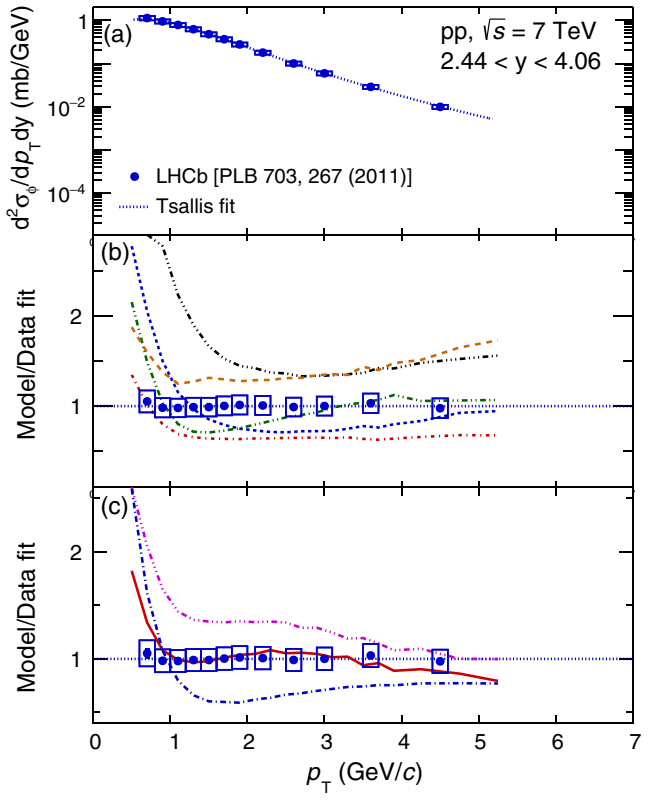

FIG. 8. Same as Fig. 4 for LHCb measurement at $\sqrt{s} = 7$ TeV [10].

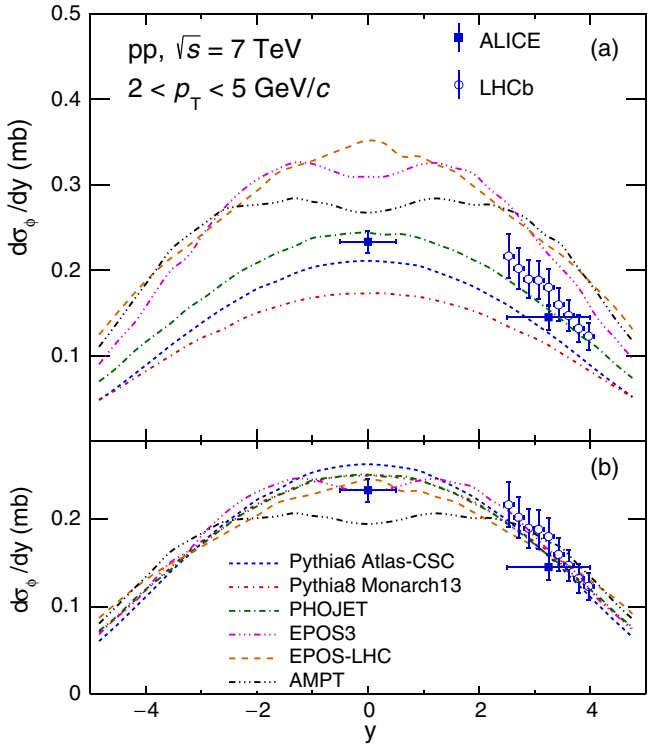

FIG. 9. $d\sigma_\phi/dy$ in $p+p$ collisions at 7 TeV and for $2 < p_T < 5$ GeV/c. (a) Comparison between LHC experiment measurements [10,12,13] and results of five simulations using PYTHIA6, PYTHIA8, PHOJET, AMPT, EPOS3, and EPOS-LHC generator models. (b) Results of the fit of the measurements using the simulated $d\sigma_\phi/dy$ shapes with normalization as the only free parameter.

integrated data points overlaid on the $d\sigma_\phi/dy$ distributions obtained using the PYTHIA6, PYTHIA8, PHOJET, EPOS3, EPOS-LHC, and AMPT models at $\sqrt{s} = 7$ TeV (a) before and (b) after the minimization procedure.

The LHC $d\sigma_\phi/dy$ at $1.2 < y < 2.2$ is calculated as the quadratic mean of the $d\sigma_\phi/dy$ from each of the model fits. The difference between the mean and the extreme value is taken as a systematic uncertainty, due to the rapidity shifting procedure, and added in quadrature to the experimental uncertainties. This uncertainty is 22.1% for the 2.76 TeV measurement and 15.5% at 7 TeV. The obtained cross sections in $1.2 < y < 2.2$ and $2 < p_T < 5$ GeV/c at LHC energies are:

(i) $\sigma_\phi(2.76\ \text{TeV}) = (1.15 \pm 0.28) \times 10^{-1}$ mb,
(ii) $\sigma_\phi(7\ \text{TeV}) = (2.23 \pm 0.35) \times 10^{-1}$ mb.

Figure 10 shows the energy dependence of the partial-ϕ-meson-production cross section integrated in $1.2 < y < 2.2$ and $2 < p_T < 5$ GeV/c in $p+p$ collisions compared to PYTHIA6, PYTHIA8, PHOJET, AMPT, EPOS3, and EPOS-LHC model predictions.

The experimental measurements follow a power-law vs the colliding energy defined as $\sigma_\phi(s) \propto s^n$, with $n = 0.43 \pm 0.03$ (black dotted line in Fig. 10). The χ^2/ndf of the power-law fit is 0.19.

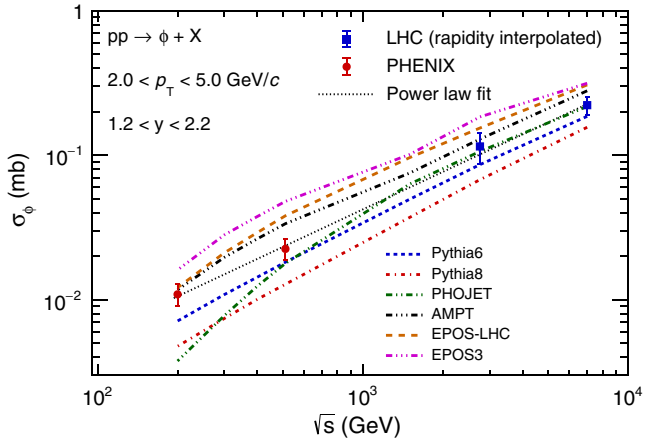

FIG. 10. Partial-ϕ-meson-production cross section in $1.2 < y < 2.2$ and $2 < p_T < 5$ GeV/c in $p+p$ collisions vs the center-of-mass energy $\sqrt{s}$ compared to different model predictions. The LHC data points are interpolated at the PHENIX forward rapidity; see the text for details.

The PHOJET generator reproduces the partial ϕ-meson cross section correctly for LHC energies but completely fails at RHIC energies. On the other hand, the AMPT model performs well at lower energies but overshoots the experimental data at 7 TeV. PYTHIA6 shows an energy dependence following a power law with exponent $n = 0.43$, comparable to that of the data, but underestimates the cross section by ~30%. Accounting for hydrodynamic evolution of the partonic system makes EPOS3 qualitatively and quantitatively more consistent with the data from both the RHIC and LHC. The increasing effect of the hydrodynamic evolution of the system on the ϕ-meson production as the energy increases can clearly be seen in Fig. 11. Also, the ϕ-meson enhancement caused by the hadronic

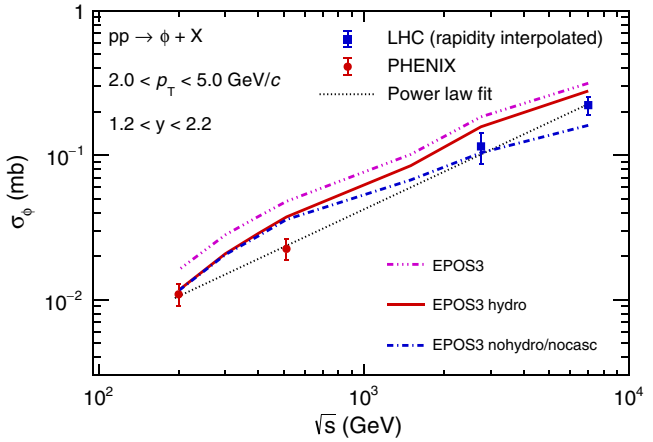

FIG. 11. Partial-ϕ-meson-production cross section in $1.2 < y < 2.2$ and $2 < p_T < 5$ GeV/c in $p+p$ collisions vs the center-of-mass energy $\sqrt{s}$ compared to the EPOS3 model using different options. The LHC data points are interpolated at the PHENIX forward rapidity; see the text for details.

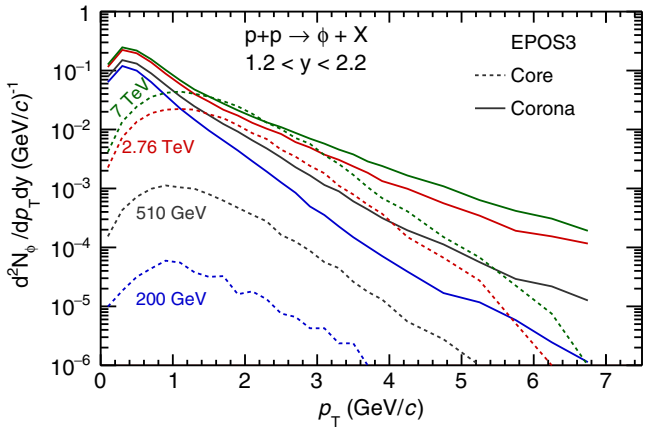

FIG. 12. Core (dashed curves) and corona (solid curves) contributions to the production of ϕ mesons in $p+p$ collisions at 0.2 (blue), 0.51 (black), 2.76 (red), and 7 TeV (green).

cascade is approximately constant over the whole energy range, ≈20%–30%.

In EPOS3, when the hydrodynamic evolution is turned off, the hadrons are produced via string decays. On the other hand, when hydrodynamic calculation is included, the various string segments originating from the initial Pomerons are separated into two collections named "core" and "corona." The core part will experience the hydrodynamic evolution, while the segments in the corona will leave the bulk matter and decay to hadrons. String segments are placed in the core or corona depending on their transverse momenta and on the local string density [34]. After its hydrodynamical evolution, the core hadronizes following the Cooper-Frye freeze-out procedure. Figure 12 shows the core and the corona contributions to the production of ϕ mesons in $p+p$ collisions for the four energies studied in this work. The contribution of the core part increases with the colliding energy, being negligible compared to the corona contribution at RHIC energies and of the same order of magnitude at LHC energies for $1 < p_T < 3$ GeV/c. The difference in the shape of the p_T distributions between the core and the corona part (shift from low to intermediate p_T) is due to the fact that in the core the ϕ mesons are produced from "fluid cells characterized by radial flow velocities" [34]. The heavier the particle is, the more transverse momentum it receives from this mechanism.

VI. SUMMARY AND CONCLUSIONS

In summary, the ϕ-meson-production differential cross section is measured in $p+p$ collisions at $\sqrt{s} = 510$ GeV in the kinematic range $1.2 < |y| < 2.2$ and $2 < p_T < 7$ GeV/c. The cross section integrated in p_T and averaged over positive and negative rapidities is $\sigma_\phi = [2.28 \pm 0.09(\text{stat}) \pm 0.14(\text{syst}) \pm 0.27(\text{norm})] \times 10^{-2}$ mb. The measured p_T-differential cross section is compared to various model predictions based on PYTHIA6, PYTHIA8, PHOJET, AMPT, EPOS3, and EPOS-LHC generators. The default AMPT model and the EPOS3 model without hadronic cascade provide the best description of the data.

The energy dependence of the ϕ-meson-production cross section is studied in the kinematic range $1.2 < y < 2.2$ and $2 < p_T < 5$ GeV/c, shifting LHC measurements to the same rapidity range as PHENIX measurements. The EPOS3 model shows that the addition of the hydrodynamic evolution of the system induces an enhancement of the ϕ-meson production at the LHC energies for $1 < p_T < 3$ GeV/c, whereas no effect is seen for RHIC energies. The LHC measurements tend to favor the scenario with the hydrodynamic evolution of the system included in EPOS3 showing a possible hint of collective effects in $p+p$ collisions at high energy.

The EPOS3 model shows that the hydrodynamic flow induces a shift from low to intermediate p_T of the produced ϕ mesons. A similar effect is obtained from tuning the color reconnection mechanism in PYTHIA8 [32,33]. The study of the $\langle p_T \rangle$ as a function of the charged particle multiplicity produced in $p+p$ collisions and its evolution vs the colliding energy would be a relevant observable of such an effect and would allow one to discriminate between alternative models. In addition to the already published data at $\sqrt{s} = 2.76$ and 7 TeV regarding the production of ϕ mesons at forward rapidity, the LHC experiments took data in $p+p$ collisions at 5, 8, and recently 13 TeV, at which the effect should be even larger.

ACKNOWLEDGMENTS

We thank the staff of the Collider-Accelerator and Physics Departments at Brookhaven National Laboratory and the staff of the other PHENIX participating institutions for their vital contributions. We also thank K. Werner and T. Pierog for their valuable help in providing the EPOS3 and EPOS-LHC software and for the fruitful discussions regarding the models. We acknowledge support from the Office of Nuclear Physics in the Office of Science of the Department of Energy, the National Science Foundation, Abilene Christian University Research Council, Research Foundation of SUNY, and Dean of the College of Arts and Sciences, Vanderbilt University (U.S.); Ministry of Education, Culture, Sports, Science, and Technology and the Japan Society for the Promotion of Science (Japan); Conselho Nacional de Desenvolvimento Científico e Tecnológico and Fundação de Amparo à Pesquisa do Estado de São Paulo (Brazil); Natural Science Foundation of China (People's Republic of China); Croatian Science Foundation and Ministry of Science and Education (Croatia); Ministry of Education, Youth and Sports (Czech Republic); Centre National de la Recherche Scientifique, Commissariat à l'Énergie Atomique, and Institut National de Physique Nucléaire et de Physique des Particules (France); Bundesministerium für Bildung

und Forschung, Deutscher Akademischer Austausch Dienst, and Alexander von Humboldt Stiftung (Germany); J. Bolyai Research Scholarship, EFOP, the New National Excellence Program (ÚNKP), NKFIH, and OTKA (Hungary); Department of Atomic Energy and Department of Science and Technology (India); Israel Science Foundation (Israel); Basic Science Research and SRC(CENuM) Programs through NRF funded by the Ministry of Education and the Ministry of Science and ICT (Korea); Physics Department, Lahore University of Management Sciences (Pakistan); Ministry of Education and Science, Russian Academy of Sciences, Federal Agency of Atomic Energy (Russia); VR and Wallenberg Foundation (Sweden); the U.S. Civilian Research and Development Foundation for the Independent States of the Former Soviet Union; the Hungarian American Enterprise Scholarship Fund; the U.S.-Hungarian Fulbright Foundation; and the U.S.-Israel Binational Science Foundation.

[1] D. Drijard *et al.* (Annecy[LAPP]-CERN-College de France-Dortmund-Heidelberg-Warsaw Collaboration), Production of vector and tensor mesons in proton proton collisions at $\sqrt{s} = 52.5$ GeV, Z. Phys. C **9**, 293 (1981).

[2] C. Daum *et al.* (ACCMOR Collaboration), Inclusive ϕ meson production in 93-GeV and 63-GeV hadron interaction, Nucl. Phys. **B186**, 205 (1981).

[3] T. Akesson *et al.* (Axial Field Spectrometer Collaboration), Inclusive vector-meson production in the central region of pp collisions at $\sqrt{s} = 63$ GeV, Nucl. Phys. **B203**, 27 (1982); Erratum, Nucl. Phys.**B229**, 541(E) (1983).

[4] G. J. Bobbink *et al.*, The production of high momentum particles and resonances in pp collisions at the CERN intersecting storage rings, Nucl. Phys. **B217**, 11 (1983).

[5] M. Aguilar-Benitez *et al.*, Inclusive particle production in 400 GeV/c pp interactions, Z. Phys. C **50**, 405 (1991).

[6] T. Alexopoulos *et al.* (E735 Collaboration), Phi meson production from p anti-p collisions at $\sqrt{s} = 1.8$ TeV, Z. Phys. C **67**, 411 (1995).

[7] S. V. Afanasiev *et al.* (NA49 Collaboration), Production of phi mesons in $p + p$, $p +$ Pb and central Pb + Pb collisions at E(beam) = 158A GeV, Phys. Lett. B **491**, 59 (2000).

[8] B. I. Abelev *et al.* (STAR Collaboration), Measurements of phi meson production in relativistic heavy-ion collisions at RHIC, Phys. Rev. C **79**, 064903 (2009).

[9] A. Adare *et al.* (PHENIX Collaboration), Measurement of neutral mesons in $p + p$ collisions at $\sqrt{s} = 200$ GeV and scaling properties of hadron production, Phys. Rev. D **83**, 052004 (2011).

[10] R. Aaij *et al.* (LHCb Collaboration), Measurement of the inclusive ϕ cross-section in pp collisions at $\sqrt{s} = 7$ TeV, Phys. Lett. B **703**, 267 (2011).

[11] K. Aamodt *et al.* (ALICE Collaboration), Strange particle production in proton-proton collisions at $\sqrt{s} = 0.9$ TeV with ALICE at the LHC, Eur. Phys. J. C **71**, 1594 (2011).

[12] B. Abelev *et al.* (ALICE Collaboration), Light vector meson production in pp collisions at $\sqrt{s} = 7$ TeV, Phys. Lett. B **710**, 557 (2012).

[13] B. Abelev *et al.* (ALICE Collaboration), Production of $K^*(892)^0$ and $\phi(1020)$ in pp collisions at $\sqrt{s} = 7$ TeV, Eur. Phys. J. C **72**, 2183 (2012).

[14] T. Aaltonen *et al.* (CDF Collaboration), Production of K^0_S, $K^{*\pm}(892)$ and $\phi^0(1020)$ in minimum bias events and K^0_S and Λ^0 in jets in $p\bar{p}$ collisions at $\sqrt{s} = 1.96$ TeV, Phys. Rev. D **88**, 092005 (2013).

[15] A. Adare *et al.* (PHENIX Collaboration), Low-mass vector-meson production at forward rapidity in $p + p$ collisions at $\sqrt{s} = 200$ GeV, Phys. Rev. D **90**, 052002 (2014).

[16] G. Aad *et al.* (ATLAS Collaboration), The differential production cross section of the ϕ (1020) meson in $\sqrt{s} =$ 7 TeV pp collisions measured with the ATLAS detector, Eur. Phys. J. C **74**, 2895 (2014).

[17] J. Adam *et al.* (ALICE Collaboration), ϕ-meson production at forward rapidity in p-Pb collisions at $\sqrt{s_{NN}} = 5.02$ TeV and in pp collisions at $\sqrt{s} = 2.76$ TeV, Phys. Lett. B **768**, 203 (2017).

[18] J. Adam *et al.* (ALICE Collaboration), $K^*(892)^0$ and $\phi(1020)$ meson production at high transverse momentum in pp and Pb-Pb collisions at $\sqrt{s_{NN}} = 2.76$ TeV, Phys. Rev. C **95**, 064606 (2017).

[19] S. Okubo, Phi meson, and unitary symmetry model, Phys. Lett. **5**, 165 (1963).

[20] G. Zweig, An SU(3) model for strong interaction symmetry and its breaking, version 1, CERN Report No. CERN-TH-401, 1964.

[21] J. Iizuka, Systematics, and phenomenology of meson family, Prog. Theor. Phys. Suppl. **37**, 21 (1966).

[22] B. Abelev *et al.* (ALICE Collaboration), Multi-strange baryon production in pp collisions at $\sqrt{s} = 7$ TeV with ALICE, Phys. Lett. B **712**, 309 (2012).

[23] V. Khachatryan *et al.* (CMS Collaboration), Strange particle production in pp collisions at $\sqrt{s} = 0.9$ and 7 TeV, J. High Energy Phys. 05 (2011) 064.

[24] P. Skands, S. Carrazza, and J. Rojo, Tuning PYTHIA8.1: The Monash 2013 tune, Eur. Phys. J. C **74**, 3024 (2014).

[25] V. Khachatryan *et al.* (CMS Collaboration), Observation of long-range near-side angular correlations in proton-proton collisions at the LHC, J. High Energy Phys. 09 (2010) 091.

[26] V. Khachatryan *et al.* (CMS Collaboration), Measurement of Long-Range Near-Side Two-Particle Angular Correlations in pp Collisions at $\sqrt{s} = 13$ TeV, Phys. Rev. Lett. **116**, 172302 (2016).

[27] G. Aad *et al.* (ATLAS Collaboration), Observation of Long-Range Elliptic Azimuthal Anisotropies in $\sqrt{s} = 13$ and 2.76 TeV pp Collisions with the ATLAS Detector, Phys. Rev. Lett. **116**, 172301 (2016).

[28] V. Khachatryan *et al.* (CMS Collaboration), Evidence for collectivity in pp collisions at the LHC, Phys. Lett. B **765**, 193 (2017).
[29] W. Li, Observation of a 'Ridge' correlation structure in high multiplicity proton-proton collisions: A brief review, Mod. Phys. Lett. A **27**, 1230018 (2012).
[30] A. Dumitru, K. Dusling, F. Gelis, J. Jalilian-Marian, T. Lappi, and R. Venugopalan, The ridge in proton-proton collisions at the LHC, Phys. Lett. B **697**, 21 (2011).
[31] P. Bozek, Elliptic flow in proton-proton collisions at $\sqrt{s} = 7$ TeV, Eur. Phys. J. C **71**, 1530 (2011).
[32] C. Bierlich and J. R. Christiansen, Effects of color reconnection on hadron flavor observables, Phys. Rev. D **92**, 094010 (2015).
[33] T. Martin, P. Skands, and S. Farrington, Probing collective effects in hadronisation with the extremes of the underlying event, Eur. Phys. J. C **76**, 299 (2016).
[34] K. Werner, B. Guiot, I. Karpenko, and T. Pierog, Analysing radial flow features in $p-$Pb and $p-p$ collisions at several TeV by studying identified particle production in EPOS3, Phys. Rev. C **89**, 064903 (2014).
[35] J. Rafelski and B. Müller, Strangeness Production in the Quark-Gluon Plasma, Phys. Rev. Lett. **48**, 1066 (1982).
[36] A. Shor, φ-Meson Production as a Probe of the Quark-Gluon Plasma, Phys. Rev. Lett. **54**, 1122 (1985).
[37] P. Koch, B. Müller, and J. Rafelski, Strangeness in relativistic heavy ion collisions, Phys. Rep. **142**, 167 (1986).
[38] T. Sjöstrand and P. Z. Skands, Transverse-momentum-ordered showers and interleaved multiple interactions, Eur. Phys. J. C **39**, 129 (2005).
[39] F. W. Bopp, R. Engel, and J. Ranft, Rapidity gaps, and the PHOJET Monte Carlo, in *High Energy Physics. Proceedings, LAFEX International School, Session C, Workshop on Diffractive Physics, LISHEP'98, Rio de Janeiro, Brazil, February 16-20* (1998), p. 729, http://inspirehep.net/record/971105.
[40] T. Pierog, I. Karpenko, J. M. Katzy, E. Yatsenko, and K. Werner, EPOS LHC: Test of collective hadronization with data measured at the CERN Large Hadron Collider, Phys. Rev. C **92**, 034906 (2015).
[41] Z.-W. Lin, C. M. Ko, B.-A. Li, B. Zhang, and S. Pal, A multi-phase transport model for relativistic heavy ion collisions, Phys. Rev. C **72**, 064901 (2005).
[42] K. Adcox *et al.* (PHENIX Collaboration), PHENIX detector overview, Nucl. Instrum. Methods Phys. Res., Sect. A **499**, 469 (2003).
[43] A. Adare *et al.* (PHENIX Collaboration), ϕ meson production in d+Au collisions at $\sqrt{s_{NN}} = 200$ GeV, Phys. Rev. C **92**, 044909 (2015).
[44] A. Adare *et al.* (PHENIX Collaboration), ϕ meson production in the forward/backward rapidity region in Cu + Au collisions at $\sqrt{s_{NN}} = 200$ GeV, Phys. Rev. C **93**, 024904 (2016).
[45] T. Sjöstrand, S. Mrenna, and P. Z. Skands, PYTHIA 6.4 physics and manual, J. High Energy Phys. 05 (2006) 026.
[46] R. Brun, F. Carminati, and S. Giani, GEANT detector description and simulation tool, CERN Report No. CERN-W-5013, 1994.
[47] K. A. Olive *et al.* (Particle Data Group), Review of particle physics, Chin. Phys. C **38**, 090001 (2014).
[48] A. Adare *et al.* (PHENIX Collaboration), Cross Section and Parity Violating Spin Asymmetries of $W^{\pm}$ Boson Production in Polarized $p + p$ Collisions at $\sqrt{s} = 500$ GeV, Phys. Rev. Lett. **106**, 062001 (2011).
[49] A. Adare *et al.* (PHENIX Collaboration), Inclusive cross section and double-helicity asymmetry for π^0 production at midrapidity in $p + p$ collisions at $\sqrt{s} = 510$ GeV, Phys. Rev. D **93**, 011501 (2016).
[50] T. Sjöstrand, S. Ask, J. R. Christiansen, R. Corke, N. Desai, P. Ilten, S. Mrenna, S. Prestel, C. O. Rasmussen, and P. Z. Skands, An introduction to PYTHIA 8.2, Comput. Phys. Commun. **191**, 159 (2015).
[51] H. Oide, Measurement of longitudinal spin asymmetry in production of muons from W/Z boson decays in polarized $p + p$ collisions at $\sqrt{s} = 500$ GeV with the PHENIX detector at RHIC, Ph.D. thesis, Tokyo University, 2012.
[52] R. Nisius, On the combination of correlated estimates of a physics observable, Eur. Phys. J. C **74**, 3004 (2014).
[53] G. D. Lafferty and T. R. Wyatt, Where to stick your data points: The treatment of measurements within wide bins, Nucl. Instrum. Methods Phys. Res., Sect. A **355**, 541 (1995).
[54] J. Cleymans and D. Worku, Relativistic thermodynamics: Transverse momentum distributions in high-energy physics, Eur. Phys. J. A **48**, 160 (2012).
[55] X.-N. Wang and M. Gyulassy, HIJING: A Monte Carlo model for multiple jet production in pp, pA and AA collisions, Phys. Rev. D **44**, 3501 (1991).
[56] B. Zhang, ZPC 1.0.1: A Parton cascade for ultrarelativistic heavy ion collisions, Comput. Phys. Commun. **109**, 193 (1998).
[57] B. Andersson, G. Gustafson, and B. Soderberg, A general model for jet fragmentation, Z. Phys. C **20**, 317 (1983).
[58] B. Andersson, G. Gustafson, G. Ingelman, and T. Sjöstrand, Parton fragmentation and string dynamics, Phys. Rep. **97**, 31 (1983).
[59] B.-A. Li and C. M. Ko, Formation of superdense hadronic matter in high-energy heavy ion collisions, Phys. Rev. C **52**, 2037 (1995).
[60] J. Xu and C. M. Ko, Triangular flow in heavy ion collisions in a multiphase transport model, Phys. Rev. C **84**, 014903 (2011).
[61] H. J. Drescher, M. Hladik, S. Ostapchenko, T. Pierog, and K. Werner, Parton-based Gribov-Regge theory, Phys. Rep. **350**, 93 (2001).
[62] S. A. Bass *et al.*, Microscopic models for ultrarelativistic heavy ion collisions, Prog. Part. Nucl. Phys. **41**, 255 (1998).
[63] M. Bleicher *et al.*, Relativistic hadron hadron collisions in the ultrarelativistic quantum molecular dynamics model, J. Phys. G **25**, 1859 (1999).

Correction: Duplication of the title introduced at the final production stage has been corrected.